Infrared-active optical phonons and magnetic excitations in the hexagonal manganites RMnO$_3$ (R = Ho, Er, Tm, Yb, and Lu)

R. Basistyy,[*] T. N. Stanislavchuk, and A. A. Sirenko
Department of Physics, New Jersey Institute of Technology, Newark, New Jersey 07102, USA

A. P. Litvinchuk
Texas Center for Superconductivity and Department of Physics, University of Houston, Houston, Texas 77204, USA

M. Kotelyanskii
Rudolph Technologies Inc., Flanders, New Jersey 07836, USA

G. L. Carr
National Synchrotron Light Source, Brookhaven National Laboratory, Upton, New York 11973, USA

N. Lee, X. Wang, and S.-W. Cheong
Rutgers Center for Emergent Materials and Department of Physics and Astronomy, Rutgers University, Piscataway, New Jersey 08854, USA

Optical properties of hexagonal multiferroic oxides RMnO$_3$, where R = Ho, Er, Tm, Yb, and Lu, have been studied in the far-infrared spectral range between 100 and 2000 cm^{-1} and temperatures between 1.5 and 300 K by means of several experimental techniques: Mueller matrix spectroscopic ellipsometry, rotating analyzer ellipsometry, and optical transmission spectroscopy. Spectra of the optical phonons are described in terms of the temperature dependencies of their frequency, damping, and oscillator strength. For all studies, oxide materials' clear signatures of the spin-phonon interaction have been found below the temperature of the antiferromagnetic phase transition T_N due to magnetic ordering of Mn^{3+} spins. A decrease of the ionic radius for R^{3+} ions between Ho^{3+} and Lu^{3+} in the corresponding RMnO$_3$ compounds resulted in systematic variation of the frequency for several optical phonons. A magnetic excitation at ∼190 cm^{-1} was observed at low temperatures below T_N and interpreted as resulting from two-magnon absorption.

I. INTRODUCTION

A. Structural and magnetic properties of hexagonal RMnO$_3$

Multiferroic rare-earth (R) manganites RMnO$_3$ (R = Ho, . . . Lu, and Sc, Y) are one of the most investigated systems inside a broader class of hexagonal (h) materials [1–9]. One of the striking peculiarities of h-RMnO$_3$ is the ferroelectric (FE) order with a large remnant polarization and high FE transition temperature T_C in the range between 600 and 1000 K [10,11]. The RMnO$_3$ hexagonal structure consists of close-packed layers of MnO$_5$ bipyramids, which share corners in the ab planes. Along the hexagonal c axis, the layers of MnO$_5$ are well separated by the R^{3+} ions. A cooperative tilting of the bipyramidal sites below T_C displaces the R^{3+} ions along the c axis into two nonequivalent sites (Wyckoff positions $2a$ and $4b$ within the $P6_3cm$ space group). Two of the R^{3+} ions within the unit cell move up (down), and one down (up), producing a ferroelectric state. The oxygen ions are also displaced in the ab plane. Both displacements of R^{3+} ions and oxygen contribute to the FE polarization [12]. Figure 1 shows schematics of the h-RMnO$_3$ crystal structure in the ferroelectric phase. More detailed discussion of the ionic displacements in the FE phase can be found in Refs. [2,12,13].

Phonon excitations in h-RMnO$_3$ (R = Y, Ho, Er, Yb, Lu) have been studied earlier using Raman scattering [12,14–28],

infrared (IR) reflectance [14,23,29,30], IR absorption [12,30], terahertz (THz) time-domain [8], and femtosecond pump-probe [31] spectroscopic techniques. Lattice dynamics of RMnO$_3$ compounds were also analyzed theoretically using shell model calculations [12,23,29], Heisenberg and the transverse Ising model [32,33], and first-principles calculations [34,35]. For the unit cell with 6 formula units (30 ions), the theory predicts 90 zone-center phonon modes. Three of them are acoustic ($A_1 + E_1$), 67 are Raman active ($9A_1 + 14E_1 + 15E_2$), and 37 are IR active ($9A_1 + 14E_1$). The remaining modes are silent (A_2, B_1, and B_2). Temperature dependence of some phonon modes was shown to exhibit anomalies near the temperature of antiferromagnetic (AFM) magnetic ordering of Mn^{3+} ions T_N, thus reflecting either atomic displacements [22] or spin-lattice interaction [15,18–23,27,29,30] below T_N. Dependence of phonon spectra on rare-earth ions was studied in bulk crystals [17] and thin films [25].

The optical phonon spectra and their temperature dependencies cannot be understood without taking into account the magnetic structure and its changes with temperature. The magnetic structure of the h-RMnO$_3$ compounds have been studied in a number of publications [13,36–39]. However, the most intriguing aspect of the magnetic interaction between Mn^{3+} and R^{3+} spins at low temperatures and high magnetic fields is still under debate [40,41]. The commonly accepted view on the magnetic structure and the corresponding magnetic phase transitions is the following: An AFM order of the Mn^{3+} spins occurs at much lower temperatures compared to the FE
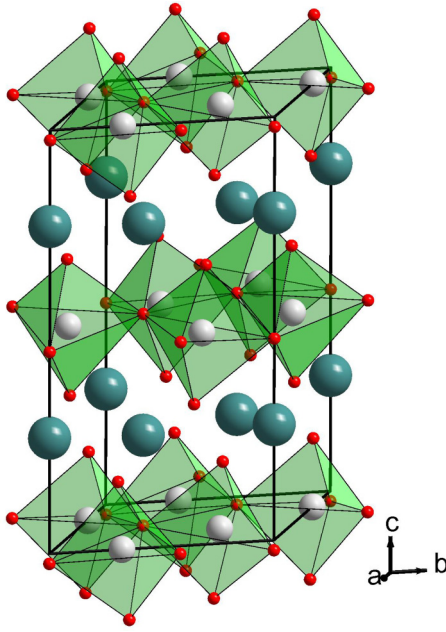

FIG. 1. (Color online) Crystal structure of hexagonal rare-earth manganites RMnO$_3$ in the ferroelectric phase. View is along (110) showing two layers of MnO$_5$ trigonal bipyramids and two layers of R^{3+} ions. HoMnO$_3$ lattice parameters and internal atomic coordinates have been used.

transition. The AFM transition temperature T_N for Mn^{3+} spins is in the range between 70 and 87 K for $R =$ Y, Ho, Er, Tm, Yb, and Lu. The neighboring Heisenberg spins of the close-packed Mn^{3+} ions are AFM coupled via the oxygen ions by superexchange interaction, which gives rise to frustration effects of an ideal 120° angle structure with the space group $P6'_3c'm$. The Mn^{3+} spins are ordered perpendicular to the c axis: $\vec{S}_{Mn} \perp c$; while at low temperatures, spins of R^{3+} ions ($R =$ Ho, Er, Tm, Yb) are oriented along the c axis: $\vec{S}_R \parallel c$. R^{3+} ion spins S_R can interact among themselves and with the Mn^{3+} spins. These interactions result in a complex phase diagram in the temperature-magnetic field parameter space $T - H$ [41,42]. Among all hexagonal RMnO$_3$ compounds with $S_{RE} \neq 0$, HoMnO$_3$ is the most studied material. Its magnetic structure is particularly interesting since it shows two additional phase transitions below T_N: Mn^{3+} spin reorientation occurs at $T_{SR} \approx 40$ K, and AFM ordering of Ho^{3+} spins takes place at $T_{RE} \approx 5$ K, as observed in neutron scattering [43,44] and second-harmonic generation optical experiments [45–48]. The spin reorientation is believed to be related to the S_{Mn} rotation in the ab plane by 90°, changing the magnetic symmetry from $P6'_3c'm$ to $P6'_3cm'$. At much lower temperatures $T < T_{RE}$, another modification of the Mn spin structure occurs and restores the $P6_3cm$ symmetry. Both low-temperature transitions at T_{SR} and T_{RE} are also accompanied by a complete or partial ordering of the Ho^{3+} spins, whose structure is not yet resolved. As mentioned in Ref. [40], two possibilities are discussed in the literature for the spins of two nonequivalent Ho^{3+} sites: (i) Ho spins on the $4b$ site develop AFM order below T_{SR} while Ho spins on the $2a$ site remain paramagnetic (PM), and (ii) all Ho spins develop

AFM order below T_{SR}. In any case, there is an agreement that the Ho sublattice exhibits long-range AFM order along the c axis below $T_{RE} \approx 5$ K [40]. Magnetization of the R spins at low temperatures in other hexagonal manganites with $R =$ Er, Tm, Yb has also been studied in Refs. [49–51], where Dzyaloshinskii-Moriya (DM) interaction [52,53] was proposed as one of the mechanisms for coupling between R spins with the partial AFM order along the c axis and Mn spins that are ordered in the ab plane.

B. Motivation for studies of the optical phonons in h-RMnO$_3$

In spite of a significant amount of the recent experimental and theoretical efforts, the IR phonon spectra in h-RMnO$_3$ still remain not fully understood. Some papers have exhaustive information about one or two particular h-RMnO$_3$ compounds but they do not provide a broader view on the whole family of h-RMnO$_3$. Further, in the majority of available experimental papers, the number of observed phonons is significantly smaller than the group theory prediction, (9 modes with A_1 symmetry polarized along the c axis and 14 doubly degenerate E_1 modes polarized in the ab plane, as mentioned above). One of the possible reasons for this is that the sensitivity of conventional optical techniques, such as reflectivity and transmittivity, is not always sufficient for analysis of materials with closely spaced phonon modes that have drastically different oscillator strengths. Most of the previous phonon studies were carried out in the temperature range above the R^{3+} spin ordering transition that occurs below 5 K, thus leaving unanswered the question about the possible effect of magnetic ordering of R^{3+} ions on phonon excitations.

In this paper, we present our systematic experimental studies of the IR-active phonons in the complete set of h-RMnO$_3$ ($R =$ Ho, ... Lu) by means of one of the most sensitive optical techniques: spectroscopic ellipsometry. We complemented our ellipsometry studies with transmission measurements of the same samples in a magnetic field. These experiments provided us with additional information about weak phonon modes and answered the question about possible field-induced modifications in an external magnetic field. The low-frequency phonon spectra for YbMnO$_3$ have been measured for the temperatures above and below the AFM ordering of Yb spins $T_{RE} = 3.3$ K. This paper is a natural continuation of our recent studies of the AFM resonances and crystal-field transitions in the far-IR spectra of the same family of h-RMnO$_3$ ($R =$ Ho, ... Lu) compounds [54].

II. EXPERIMENTAL

A. Sample growth

The high-temperature flux growth technique was utilized to produce bulk crystals of RMnO$_3$ for $R =$ Er, Tm, Yb, and Lu. Single crystal platelets with pristine, or as-grown, surfaces and the hexagonal c axis perpendicular to the surface were used for both ellipsometry and transmission measurements. The ab plane surface area of the flux-grown samples was about 4×4 mm^2, and their thickness was about 0.1 mm. The opposite sides of the samples were not wedged, resulting in relatively strong thickness interference fringes in the measured optical spectra below the optical phonon frequencies. The natural

platelet shape of the Er, Tm, Yb, and Lu samples did not allow for optical measurements from the ac or bc planes. In contrast, the HoMnO$_3$ sample was grown using the floating zone technique. The sample dimensions were about $4 \times 4 \times 4$ mm^3, which allowed for the ellipsometry studies of both c axis and ab plane optical properties of HoMnO$_3$.

B. Ellipsometry technique

The rotating analyzer ellipsometry (RAE) and Mueller matrix ellipsometry (MME) measurements were carried out at U4IR beamline of the National Synchrotron Light Source, Brookhaven National Laboratory (NSLS-BNL). The ellipsometry setup, which is described in detail in Refs. [55,56], allowed us to measure the optical phonon spectra in the temperature range between 7 and 300 K in the spectral range between 100 and 2000 cm^{-1} using a spectral resolution of 0.7 cm^{-1}. This setup consists of a Bruker v66i spectrometer, several LHe-pumped ($\sim$1.6 K) and LHe 4 K bolometers, and a LHe-cooled CuGe detector. In our previous studies of the AFM resonances in the same set of hexagonal RMnO$_3$ samples, we had focused on the spectra of the AFM resonances in the far-IR spectral range below 100 cm^{-1} [54]. In this paper, our main interest is in the optical phonon spectral range above 100 cm^{-1}. The main advantage of RAE in comparison with conventional reflectivity is the possibility to measure both real and imaginary parts of the dielectric function. Mueller matrix ellipsometry is even more powerful due to the simultaneous measurement of several components of the 4×4 Mueller matrix that connects the Stokes polarization vectors for incoming $\vec{S}_{\text{IN}}$ and outgoing (reflected) light $\vec{S}_{\text{OUT}}$. For each frequency of the measured spectra, a Mueller matrix $\hat{M}(\omega)$ is defined as $\vec{S}_{\text{OUT}}(\omega) = \hat{M}(\omega) \cdot \vec{S}_{\text{IN}}(\omega)$. In the following, the experimental data will be presented in terms of the normalized Mueller matrix components $m_{ij}(\omega) = M_{ij}(\omega)/M_{11}(\omega)$ that are more robust against systematic errors due to self-normalization by the total reflected intensity that is given by the $M_{11}(\omega)$ spectrum. The measured experimental spectra of $m_{ij}(\omega)$, which vary from -1 to $+1$, contain all the information about optical phonons that can be polarized along or perpendicular to the c axis of hexagonal manganites. The angle of incidence (AOI) for the light on the sample in all ellipsometric measurements was set to 75°, close to the Brewster angle for the low-frequency spectral range of h-RMnO$_3$. In the following, we use a standard ellipsometry convention for the Cartesian x, y, z coordinate system: z is perpendicular to the reflecting surface of the sample, x is parallel, and y is, correspondingly, perpendicular to the reflection plane.

C. Transmission experiments

Transmission experiments were carried out at the same U4IR beamline of NSLS-BNL. The main goal of these complementary experiments was to measure the weak spectra of the low-frequency phonons between 100 and 200 cm^{-1} and high-frequency phonon features above 500 cm^{-1}. In addition, a possible modification of the optical phonon spectra in an external magnetic field was investigated. The experimental configuration for transmission experiments is the same as previously described in Ref. [54]. An optical Oxford magnet

TABLE I. Shell model parameters for h-RMnO$_3$.

Ion	Z (|e|)	Y (|e|)	α (Å^3)	Ionic pair	a (eV)	b (Å^{-1})	c (eV·Å^6)
R	2.85	3.10	2.33	R-O	1738	3.04	0
Mn	2.85	3.15	2.71	Mn-O	2020	3.26	0
O	1.90	1.10	2.00	O-O	22764	6.71	20.37

was used for the sample cooling and for application of an external magnetic field up to 9 T along the c axis of the samples, i.e. perpendicular to the sample surface. Correspondingly, the electric and magnetic fields of light were always in the hexagonal plane perpendicular to the c axis. The spectral range for transmission experiments in magnetic field was between 20 and 210 cm^{-1} with a spectral resolution of 0.7 cm^{-1}. The low-frequency cutoff was determined by diffraction, while the high frequencies were limited by the light absorption in the cryostat windows. The higher frequency transmission spectra above 500 cm^{-1} were measured in the same cold-finger cryostat as used for the ellipsometry measurements. For each sample, the raw data of transmitted intensity were normalized to transmission through an empty aperture with size equal to that of the sample. Polarization of the transmitted light was not analyzed due to the expected optical isotropy in the ab plane of the measured hexagonal samples.

D. Shell model lattice dynamics calculations

Lattice vibrations of h-RMnO$_3$ were calculated by means of the shell model [57], which is proven to reasonably describe the properties of ionic materials, in particular, manganese oxides [58,59]. In the shell model, each ion with the charge Z is considered as a point core with charge Y surrounded by a massless shell with charge Q. The free ion polarizability $\alpha = Y^2/k$, where k is a force constant. The short range potentials $V(r)$ are chosen in the Born-Mayer-Buckingham form $V(r) = a \cdot e^{-b \cdot r} - c/r^6$, where r is the interatomic distance, a, b, and c are the potential parameters. The cation-anion short range interactions contain no attractive part, and $c = 0$ in the expression for $V(r)$. The Coulomb energy calculations are based on a real space summation involving a spherical cutoff boundary, which is defined by the cutoff radius and set to 10 Å, making the sum of all charges within the spherical cutoff region equal to zero. The parameters of the model used for a series of h-RMnO$_3$ compounds are listed in Table I. Note that they are somewhat different from those used earlier in Ref. [23] due to a different set of R and Mn ionic charges and polarizabilities.

III. EXPERIMENTAL RESULTS

A. Phonon spectra

Figures 2(a) and 2(b) show experimental data for the real $\langle \varepsilon_1(\omega) \rangle$ and imaginary $\langle \varepsilon_2(\omega) \rangle$ parts of the pseudodielectric functions for YbMnO$_3$ measured at $T = 7$ K obtained using RAE at AOI = 75°. The optical spectra of $\langle \varepsilon_{1,2}(\omega) \rangle$ are dominated by multiple strong IR phonons that are marked in Figs. 2(a) and 2(b) with vertical arrows and labels that correspond to their frequencies in reciprocal centimeters.
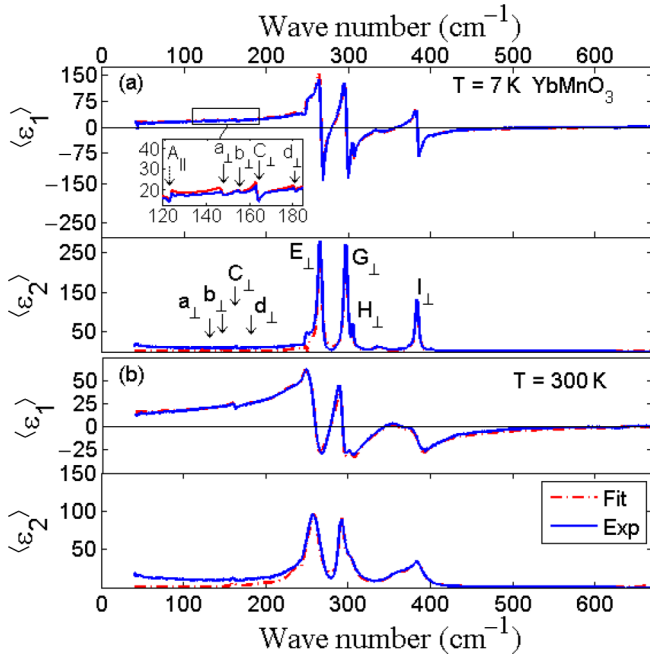
FIG. 2. (Color online) Spectra of the (a) real and (b) imaginary components of the pseudodielectric function $\langle \varepsilon_{1,2}(\omega) \rangle$ measured at $T = 7$ K for YbMnO$_3$. Strong phonons are marked with arrows and letter symbols. Solid curves correspond to the fit using Eq. (1) for the parametric description model of the dielectric function. Inset in (a) shows several phonon peaks in the low-frequency part of the spectrum.

Due to hexagonal symmetry, the dielectric function tensor is diagonal in the laboratory x, y, z coordinate system ($c \parallel z$) with only three nonzero components $\varepsilon_{xx}(\omega) = \varepsilon_{yy}(\omega) = \varepsilon_\perp(\omega)$ and $\varepsilon_{zz}(\omega) = \varepsilon_\parallel(\omega)$. At each frequency, the measured $\langle \varepsilon_{1,2}(\omega) \rangle$ is a function of $\varepsilon_\perp(\omega)$, $\varepsilon_\parallel(\omega)$, and AOI $= \phi$ [60]:

$$
\langle \varepsilon \rangle = \sin^2(\phi) \cdot \left[1 + \sin^2(\phi) \right.
$$

$$
\left. \cdot \left\{ \frac{\varepsilon_\perp \sqrt{\varepsilon_\perp - \sin^2(\phi)} - \sqrt{\frac{\varepsilon_\perp [\varepsilon_\parallel - \sin^2(\phi)]}{\varepsilon_\parallel}}}{\varepsilon_\perp \cos^2(\phi) - \sqrt{\varepsilon_\perp - \sin^2(\phi)} \cdot \sqrt{\frac{\varepsilon_\perp [\varepsilon_\parallel - \sin^2(\phi)]}{\varepsilon_\parallel}}} \right\}^2 \right].
$$

Note, however, that at AOI $= 75°$, the main contribution to the measured pseudodielectric function originates from $\varepsilon_\perp(\omega)$, while only several strong poles and zeroes of $\varepsilon_\parallel(\omega)$ appear in the spectra shown in Figs. 2(a) and 2(b), like for example the peak at ~ 125 cm^{-1}, which corresponds to the lowest frequency longitudinal optical (LO) phonon polarized along the c axis. The measured spectra were fitted using anisotropic model function consisting of two sets of Lorentz oscillators polarized along and perpendicular to the c axis

$$
\varepsilon(\omega)_\parallel = \varepsilon_{\infty,\parallel} + \sum_{n=1}^{N} \frac{S_n \cdot \omega_{n,0}^2}{\omega_{n,0}^2 - \omega^2 - i\gamma_n \omega},
$$

$$
\varepsilon(\omega)_\perp = \varepsilon_{\infty,\perp} + \sum_{m=1}^{M} \frac{S_m \cdot \omega_{m,0}^2}{\omega_{m,0}^2 - \omega^2 - i\gamma_m \omega},
\tag{1}
$$

where $\omega_{n(m),0}$ is the phonon frequency, $S_{n(m)}$ is the oscillator strength, $\gamma_{n(m)}$ stands for the phonon broadening, and $\varepsilon_{\infty,\parallel(\perp)}$ represents the dielectric constant at frequencies above the optical phonons. Due to the hexagonal symmetry, two sets of the phonon parameters $\omega_{n(m),0}$, $S_{n(m)}$, and $\gamma_{n(m)}$ are, of course, different for $\varepsilon_\parallel(\omega)$ and $\varepsilon_\perp(\omega)$. To describe the optical phonon spectra, we used $N = 6$ for phonons polarized along the c axis and $M = 13$ for phonons polarized in the ab plane. A homemade program based on the 4×4 Berreman's model for anisotropic magnetoelectric medium was used for all fits presented in this paper [61]. The results of the fit are shown in Figs. 2(a) and 2(b) with dashed red curves. The discrepancy between the fit and experimental data for the low-frequency part of $\langle \varepsilon_2(\omega) \rangle$ for $\omega < 100$ cm^{-1} is due to a systematic error of RAE. This error is caused by a well-known limitation of the RAE technique in the transparency region, where the phase of the reflected light changes upon reflection by an angle of $\sim 180°$, thus making RAE insensitive to the optical losses. In fact, $\langle \varepsilon_2(\omega) \rangle$ should be close to zero in this spectral range, as it appears in the model for the fit and as we also confirmed with our transmission measurements of the same samples in Ref. [54]. Table II summarizes the experimental values for the transverse optical (TO) phonon frequencies for all measured hexagonal manganites at $T = 7$ K. Strong phonons are labeled with capital letters C, E, . . ., while weak phonons are differentiated from them by using small letters a, b, d, . . . in alphabetic order for their frequency increase. The polarization of the phonon along or perpendicular to the c axis is marked with the corresponding symbols $\parallel$ or $\perp$.

To obtain better sensitivity to the optical phonons polarized along the c axis of hexagonal compounds, we measured a bulk HoMnO$_3$ sample with the c axis in the reflection plane ($c \parallel x$). We also utilized the MME technique, which is free from the aforementioned systematic errors of RAE for transparent samples. Another advantage of MME is the capability to measure several independent Mueller matrix components $m_{ij}(\omega)$ that are more reliable in the case of strong sample anisotropy. Figure 3 shows spectra of $m_{12}(\omega)$, $m_{33}(\omega)$, and $m_{34}(\omega)$ for the HoMnO$_3$ sample in all three possible configurations: $c \parallel x$, $c \parallel y$, and $c \parallel z$. Experimental data for all three configurations were fitted using the same self-consistent anisotropic model for the phonon parameters $\omega_{n(m),0}$, $S_{n(m)}$, and $\gamma_{n(m)}$. The results of the fit for both real and imaginary components of the anisotropic dielectric function, $\varepsilon_\perp(\omega)$ and $\varepsilon_\parallel(\omega)$, are shown in Figs. 4(a) and 4(b).

Several low-frequency modes polarized in the ab plane at about 145, 155, and 185 cm^{-1} are not clearly resolved in ellipsometric spectra, especially at high temperatures above 200 K. The corresponding peaks shown in Fig. 5(a) for YbMnO$_3$ have an electric dipole shape, as expected for phonons, but their strength decreased significantly in the PM phase for $T > T_N$, thus leaving room for other interpretations, such as modes of magnetic origin or crystal field transitions. To support their interpretation as phonons, we used a complementary transmission technique that for the given sample thickness turns out to be more sensitive to the weak excitations. The corresponding spectra are shown in Fig. 5(b) for YbMnO$_3$. The absorption peaks appeared in the transmission spectra at the same frequencies as in the ellipsometry spectra. These peaks were also observed in the temperature range much higher

TABLE II. Experimental TO phonon frequencies ω_0 with the E_1 symmetry polarized in the ab plane for h-RMnO$_3$ in reciprocal centimeters for $T = 7$ K. Strong and weak modes are marked with small and capital letters, respectively. Frequencies of the magnetic excitations (Mag) and crystal field (CF) transition are listed at the bottom.

Number (m)	Letter symbol	HoMnO$_3$	ErMnO$_3$	TmMnO$_3$	YbMnO$_3$	LuMnO$_3$
1	A		147.9	146.0	147.4	147.1
2	b	151.5	154		155.3	155.5
3	C	165.5	164.6	163.7	163.5	162.1
4	D		184.5	179.8	181.4	182.4
5	E	245	254.5	257.5	265.4	270.5
6	f	266.5	270.5		267.5	273.5
7	G	292.5	294.6	295	297.2	303.3
8	h	308	311	301	305.5	313
9	I	368	371	372	383.5	368
10	j		408			415
11	K	420	421	422		428
12	l		522	526	526	528
13	m	591	594			600
Mag				180	190	191
				193		210
CF			366			

than the AFM-PM phase transition $T_N = 84$ K for YbMnO$_3$ and other compounds. Figures 5(c), 6(a), and 6(b) show a number of transmission maps for YbMnO$_3$, LuMnO$_3$, and TmMnO$_3$ in the frequency-temperature space, where most of the weak phonon peaks at 145, 155, and 185 cm^{-1} are clearly visible up to ∼200 K, thus unambiguously confirming their phonon origin. Additional confirmation that those peaks are not R^{3+} crystal field transitions came from the measurements of LuMnO$_3$, where the $4f$ shell of R^{3+} is complete and no crystal field transitions are expected [see Fig. 6(a)]. Thus,

observation of the low-frequency modes, such as the ones at 144, 155, 165, and 180 cm^{-1}, can be significantly improved in transmission configuration when the thickness of the sample can compensate for the weak absorption by the modes. Note that this approach works well only if the sample is nearly transparent in the frequency range of interest. In other words, the background values of the dielectric function should be $\varepsilon_1(\omega) \gg 1$ and $\varepsilon_2(\omega) \approx 0$. These conditions have been naturally realized in the low-frequency range of h-RMnO$_3$ below the strong phonon absorption.
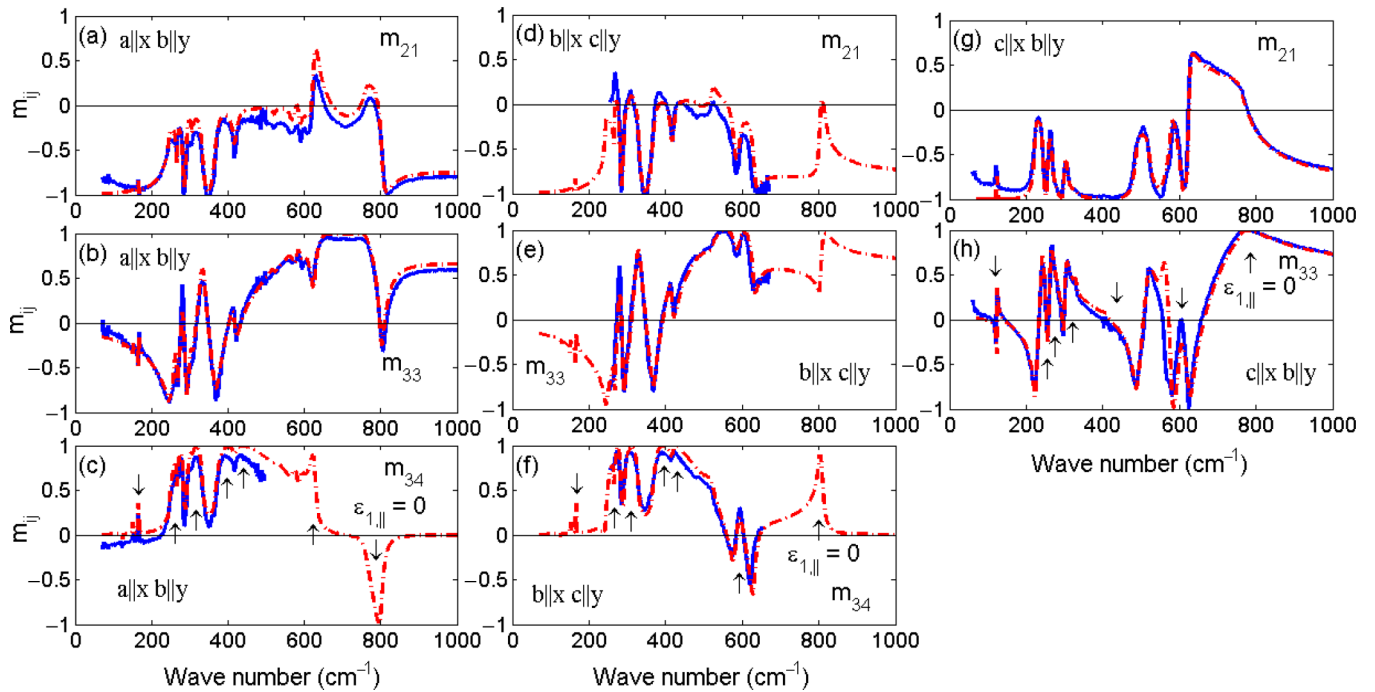

FIG. 3. (Color online) Spectra of the normalized Mueller matrix components $m_{12}(\omega)$, $m_{33}(\omega)$, and $m_{34}(\omega)$ (blue curves) for the same HoMnO$_3$ sample at $T = 7$ K in three experimental configurations (a)–(c) $c \parallel z$, (d)–(f) $c \parallel y$, and (g), (h) $c \parallel x$. The results of the fit are shown with dashed red curves.
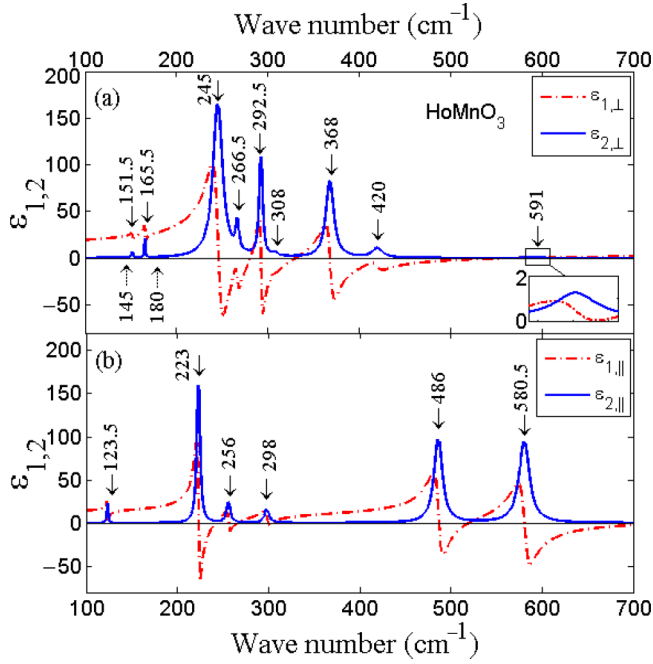
FIG. 4. (Color online) Anisotropic dielectric function model for the HoMnO$_3$ sample calculated with experimental parameters from Tables II and III obtained for $T = 7$ K. (a) $\varepsilon_\perp(\omega)$ and (b) $\varepsilon_\parallel(\omega)$. Real part is shown with red and imaginary parts are shown with blue curves. The strongest optical phonons are marked with arrows.
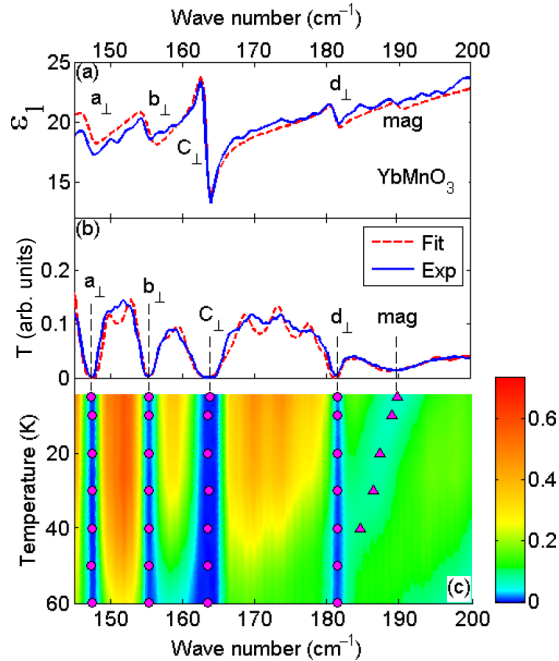

FIG. 5. (Color online) (a) Experimental RAE data (blue curve) for the real part of the pseudodielectric function $\langle \varepsilon_1(\omega) \rangle$ measured at $T = 7$ K for YbMnO$_3$. The phonon peaks are marked with arrows. The fit results are shown with a red curve. (b) Transmittivity spectra for the same YbMnO$_3$ sample for $T = 7$ K. (c) Transmittivity $\omega - T$ map for the same YbMnO$_3$ sample. The results of the fit for the phonon frequency are shown with circles. The magnetic mode at 190 cm^{-1} that is visible only at $T < 50$ K is marked with triangles.
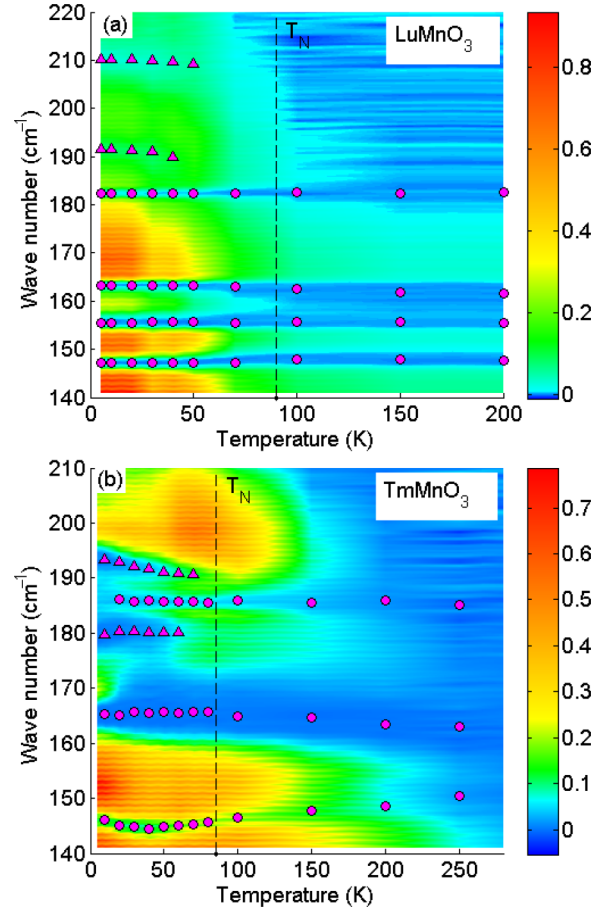

FIG. 6. (Color online) Transmittivity $\omega - T$ maps for (a) LuMnO$_3$ and (b) TmMnO$_3$. The results of the fit for the phonon frequency are shown with circles. Note that the weak optical phonons at ~ 148, 154, and 185 cm^{-1} are visible in the temperature range well above T_N shown with dashed vertical lines in both (a) and (b). The magnetic modes at 190 and 210 cm^{-1} in (a) and 180 and 193 cm^{-1} in (b) are shown with triangles.

B. Temperature dependence of the phonon frequencies

Temperature dependencies of all optical phonon frequencies are shown in Figs. 7(a)–7(k) for the phonons polarized in the *ab* plane. Data for all five measured hexagonal compounds with $R =$ Ho, Er, Tm, Yb, and Lu are presented together for comparison. Each panel of Fig. 7 corresponds to the same mode of the hexagonal structure. As one can see in both Figs. 7(c), 7(e), and 7(g) and Table II, several strong low-frequency phonons reveal systematic trends of their frequencies. Thus, the strong $C_\perp$ mode at ~ 163 cm^{-1}, which is predominantly determined by displacements of the heavy R^{3+} ions, reveals a systematic decrease of the frequency for R^{3+} ions between Ho^{3+} and Lu^{3+} [see Fig. 7(c)]. This "classical" trend is illustrated in Fig. 8 using a linear fit between the square root of the inverted mass $M_{R^{3+}}$ of the R^{3+} ions and the phonon frequency. The error bars in Fig. 8 are determined predominantly by the resolution of our spectrometer. Another two strong $E_\perp$ and $G_\perp$ phonons at 260 and 300 cm^{-1} also show a systematic variation of their frequency, but with an opposite trend [see Figs. 9(a) and 9(b)]. A well-known decrease of the ionic radius for R^{3+} ions between Ho^{3+} and Lu^{3+}
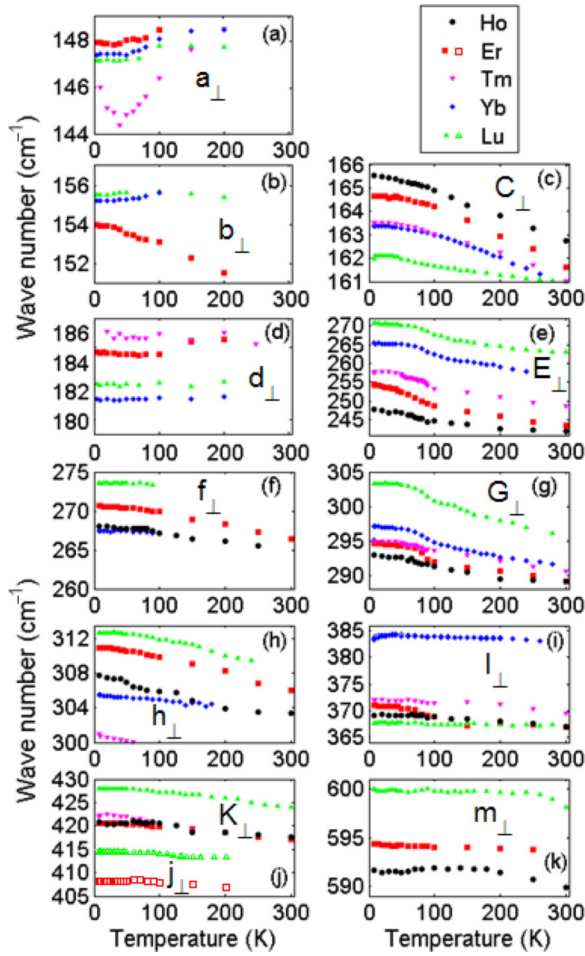
FIG. 7. (Color online) Temperature dependence of the frequency for the TO phonons polarized in the *ab* plane for $RMnO_3$, $R = $ Ho (black circles), Er (red squares), Tm (pink down triangles), Yb (blue diamonds), and Lu (green up triangles). Letters correspond to the phonon notation in Table II. (a) $a_\perp$, (b) $b_\perp$, (c) $C_\perp$, (d) $d_\perp$, (e) $E_\perp$, (f) $F_\perp$, (g) $G_\perp$, (h) $H_\perp$, (i) $I_\perp$, (j) open symbols $j_\perp$, solid symbols $K_\perp$, and (k) $m_\perp$.
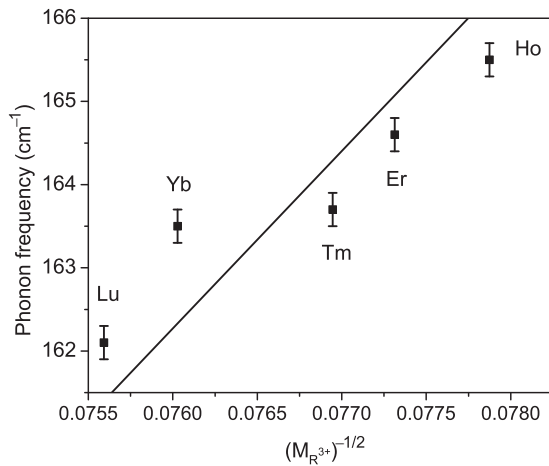

FIG. 8. A quasilinear increase of the optical phonon frequency for the $RMnO_3$ compounds. Experimental data points were measured at $T = 7$ K. The solid line is a linear fit using $\omega_0 \sim 1/\sqrt{M_{R^{3+}}}$, where M is in atomic units.
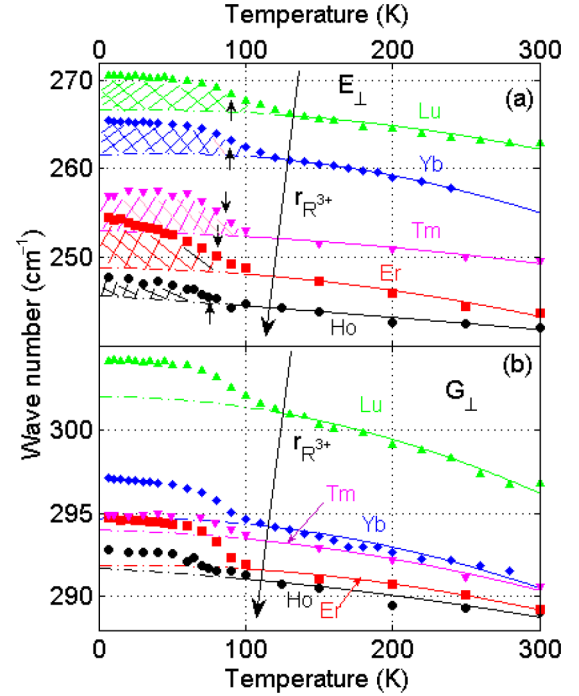

FIG. 9. (Color online) Temperature dependence of the frequency for two *ab* plane E_1-symmetry optical phonons with the strongest spin-phonon interaction for $RMnO_3$, $R = $ Ho (black circles), Er (red squares), Tm (pink down triangles), Yb (blue diamonds), and Lu (green up triangles). (a) $E_\perp$ and (b) $G_\perp$ phonons. The AFM ordering temperature for Mn^{3+} spins is shown in (a) with small black vertical arrows. The long black arrows in both (a) and (b) show schematically an increase of the R^{3+} ionic radius r_{R3+} from Lu to Ho. Solid curves are fits using Eq. (2) for the high-temperature part of the $\omega_0(T)$ dependence. Dashed curves correspond to extrapolation of Eq. (2) to low temperatures. The discrepancy between experimental data points and dashed curves that is highlighted with the cross-hatched areas in (a) is due to spin-phonon interaction.

in the $RMnO_3$ compounds seems to be a dominant factor for the qualitative explanation of the systematic changes of these two midfrequency phonons. The other high-frequency (>350 cm^{-1}) phonons, which are associated with vibrations of the lighter ions (oxygen and manganese), are less sensitive to the properties of the R^{3+} ions and their frequencies vary rather randomly among different $RMnO_3$ compounds.

Most of the phonons have weak frequency dependence at $T < 95$ K and a typical decrease of their frequency with the quasilinear slope for $T > 120$ K. This natural softening of the optical modes with the temperature increase is known to be caused by the thermal expansion of the lattice and anharmonic phonon-phonon interactions, which become more important as the temperature increases due to the statistical increase of the number of phonons. We calculated the temperature dependence of several phonons using the following equation [62]:

$$\omega_0(T) = \omega_{0|T=0} \times \exp\left[-3\gamma_G \int_0^T \alpha(T')dT'\right], \quad (2)$$

where γ_G is a Grüneisen parameter, $\alpha(T)$ is the linear expansion coefficient obtained from Ref. [42], and $\omega_{0|T=0}$ is
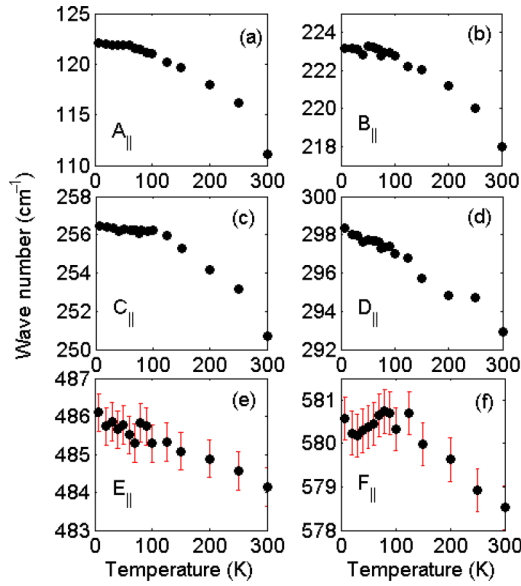
FIG. 10. (Color online) Temperature dependence of the frequency for the c axis polarized optical phonons in HoMnO$_3$. (a) $A_\parallel$, (b) $B_\parallel$, (c) $C_\parallel$, (d) $D_\parallel$, (e) $E_\parallel$, (f) $F_\parallel$. The error bars in (e) and (f) show the fit accuracy for relatively broad high-frequency modes. The low-frequency phonons are much sharper and, hence, the accuracy of the fit is comparable with the symbol size that is about 0.3 cm^{-1}. The anomaly in the temperature dependence for $F_\parallel$ mode in (f) is close to the AFM ordering temperature for Mn^{3+} spins $T_N = 75$ K.

FIG. 11. (Color online) Magnetic field dependence of the transmittivity $\omega - H$ map measured in YbMnO$_3$. (a) $T = 5$ K and (b) $T = 1.5$ K. The optical phonon peaks are marked with diamonds. The magnetic peaks at ~ 190 cm^{-1} are marked with open squares. (c) Magnetic field dependence of the peak at ~ 190 cm^{-1} for two temperatures 1.5 and 5 K. Solid lines in (c) guide the eye.

the phonon frequency at zero temperature. The results of the calculation using $\gamma_G = 0.7 \pm 0.2$ are shown in Figs. 9(a) and 9(b) with solid curves.

While most of the phonons can be well described by Eq. (2) for their $\omega_0(T)$ in the whole temperature range between 7 and 300 K, several phonons show strong anomalies at T_N for AFM ordering of Mn^{3+} spins. The corresponding dependencies are shown in Figs. 9(a) and 9(b) for the $E_\perp$ and $G_\perp$ modes at ~ 260 and ~ 300 cm^{-1}. Below T_N, their frequencies increase by $\Delta\omega(T)$, which is equal to several wave numbers (3 cm^{-1} for the phonon at 300 cm^{-1} and 5 cm^{-1} for the phonon at 260 cm^{-1}) above the level predicted by the Grüneisen formula. This difference is highlighted by the dashed region in Fig. 9(a). The non-Grüneisen behavior can be attributed to the strong spin-phonon interaction that emerged in the low temperature AFM phase. It is natural that this effect is expected to be the most pronounced for those phonon modes, whose atomic displacements effectively modulate the Mn-Mn exchange interaction (see, e.g. Ref. [63] and references therein). The weakest effect in terms of the $\Delta\omega(T)$ values at low temperature has been observed in HoMnO$_3$ $\Delta\omega(7K) \approx 1.5$ cm^{-1}, while in other compounds with $R =$ Er, Tm, Yb, and Lu $\Delta\omega(7K)$ turns out to be close to 5 cm^{-1} for the mode at 300 cm^{-1}. Similar trends for the temperature dependence of the phonon frequencies at ~ 260 and ~ 300 cm^{-1} have been previously observed in the Raman spectra and reflectivity experiments in Refs. [20,23].

Temperature dependence of the optical phonons in HoMnO$_3$ polarized along the c axis is shown in Fig. 10. The total number of the measured modes is six, smaller than that
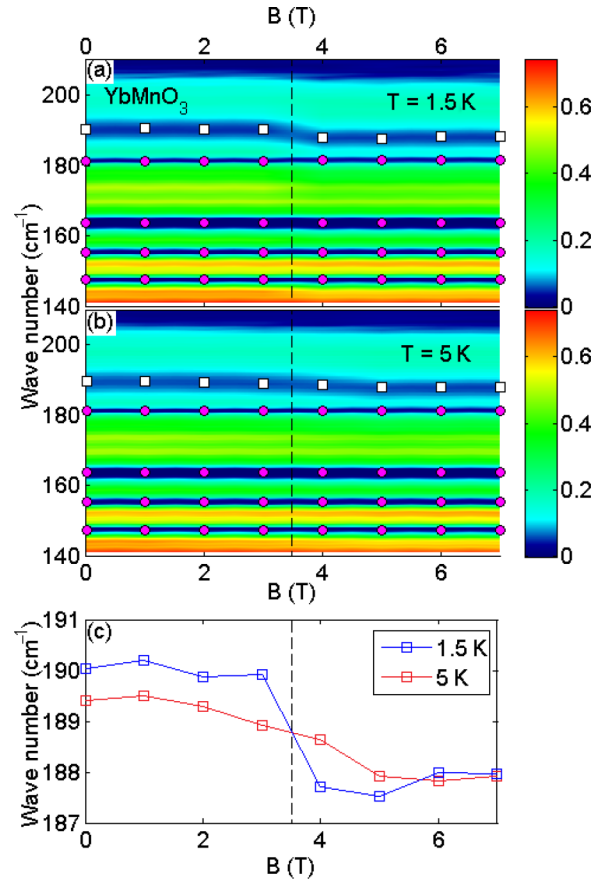
for the ab plane phonons. Our measurement did not reveal any significant spin-phonon interaction anomalies for this phonon polarization except for a small decrease of the $F_\parallel$ mode frequency for temperatures below $T_N = 75$ K. This decrease of ~ 1 cm^{-1} exceeds only slightly the error bars for the measured phonon frequencies.

C. Transmission spectra in the magnetic field

Figures 11(a) and 11(b) show $\omega - H$ maps of transmittivity measured in YbMnO$_3$ at $T = 1.5$ and 5 K. The positions of the phonon peaks at 144, 155, 165, and 180 cm^{-1} do not show any measurable changes with the strong magnetic field directed along the c axis. In addition to the phonons, one can see a broader peak at 190 cm^{-1}. This peak is only observed for temperatures below $T_N = 84$ K [see Fig. 11(c)]. Note that the broadening of the magnetic peaks exceeds significantly that of the phonons in the same frequency range. The magnetic-field-induced softening measured at $T = 5$ K indicates a magnetic origin of these excitations. In addition to YbMnO$_3$, a similar broad peak at 190 cm^{-1} was also observed in TmMnO$_3$ and LuMnO$_3$ indicating the Mn^{3+} spin system to be at the origin of this particular excitation and excluding interpretations

related to the crystal field transitions. The magnetic peak frequencies are summarized in Table II. The commonly accepted model for a 120° spin structure for Mn^{3+} ions in h-RMnO$_3$ does not include any single-particle excitations at the center of the Brillouin zone $\vec{k} = 0$ and polarized in the ab plane other than the doubly degenerate AFM resonance peak, whose frequency is between 40 and 50 cm^{-1} depending on the R^{3+} ion [64]. This prediction has been confirmed by both IR transmission [54] and recent neutron scattering experiments [65]. Thus, the most plausible interpretation of the observed magnetic peak at 190 cm^{-1} is related to two-magnon absorption. According to Ref. [65], the maximum of the two-magnon density of states in h-RMnO$_3$ is close to 200 cm^{-1}, which is consistent with the observed position of our peak at 190 cm^{-1}.

For the temperatures below the rare-earth spin ordering $T_{Yb3+} = 3.3$ K [54], the magnetic field dependence of the peak at 190 cm^{-1} changes. One can see a steplike behavior at the field of about 3.5 T in Fig. 11(c). The position of this peak suddenly decreases by about 2 cm^{-1} when the magnetic field exceeds $\sim$3.5 T. We observed a qualitatively similar, i.e. steplike, behavior recently for the AFM resonance peak at 53 cm^{-1} in the same YbMnO$_3$ crystal measured for $T < T_{Yb3+}$ [54]. Several papers report critical endpoint behavior of magnetic spin system in h-RMnO$_3$ at magnetic fields close to 3 T and temperatures below the spin orientation for R^{3+} ions $T < T_{R3+}$ [66]. In a simplified quantitative picture such steps in magnetic-field dependencies are usually attributed to the internal fields associated with orientation of Yb^{3+} spins to the direction of the magnetic field (the c axis) and simultaneous in-plane reorientation of Mn^{3+} spins.

In TmMnO$_3$, the magnetic peak has been observed at 193 cm^{-1}. The frequency of this peak softens under increase of both the magnetic field and temperature. This peak disappears above $T_N = 82$ K for Mn^{3+} ions. The softening of the magnetic peak under application of external magnetic field results in its downshift to $\sim$190 cm^{-1} and disappearance in
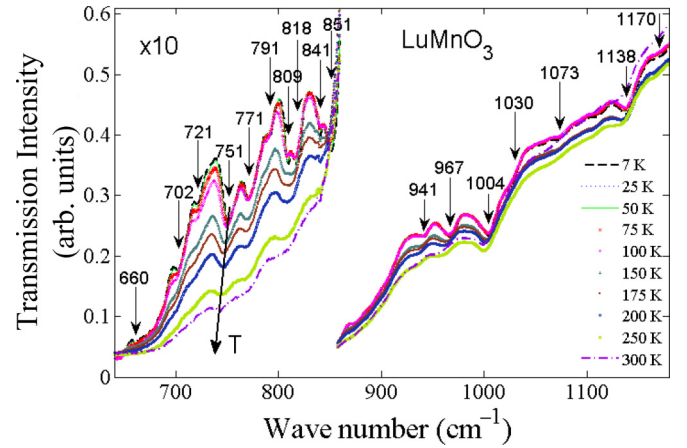

FIG. 12. (Color online) Transmittivity spectra for LuMnO$_3$ dominated by absorption peaks due to the two- and three-phonon density of states. The minimum of transmitted intensity below 650 cm^{-1} is due to the bremsstrahlung band. The phonon-related absorption features are marked with vertical arrows. Note the softening and broadening of the phonon absorption features with the temperature increase that is highlighted with inclined arrow at 751 cm^{-1}.

the fields above 4 T. No steplike behavior was observed at low temperatures down to 1.5 K, probably due to the even lower T_{Tm3+} temperature.

D. Transmission spectra and multiphonon absorption

For the high-frequency range, the transmission configuration is not that useful as it appears for the spectra below 200 cm^{-1}. For example, all phonons that are above 400 cm^{-1} and are polarized in the ab plane fall into the bremsstrahlung band 370–580 cm^{-1} with $\varepsilon_1(\omega) \ll 0$. As a result, the reflectivity of the sample is close to 1 in that frequency range and the remaining transmitted intensity is

TABLE III. Calculated and experimental parameters of TO phonons with the E_1 symmetry for h-HoMnO$_3$ polarized in the ab plane for $T = 7$ K.

Number (m)	Calculation ($\omega_{0,m}$)	S_m	Letter symbol	Experiment ($\omega_{0,m}$)	HoMnO$_3$ (γ_m)	S_m
1	125	0.1	a			
2	166	0.001	b	151.5	1.6	0.07
3	196	0.001	C	165.5	1.0	0.12
			d			
4	276	0.01	E	245	12.0	8.0
			f	266.5	4.1	0.4
5	286	0.14	G	292.5	4.1	1.5
			h	308	7.1	0.08
6	370	2.89	I	368	10.1	2.2
7	398	0.02	j			
8	415	0.04				
9	429	0.18	K	420	13.7	0.3
10	561	0.35	L			
11	570	1.55				
12	571	0.001	m	591	14.8	0.03
13	609	0.001				
14	667	0.02				

$\varepsilon_{\infty,\perp} = 4.75$

TABLE IV. Calculated and experimental parameters of TO phonons with the A_1 symmetry for h-HoMnO$_3$ polarized along the c axis for $T = 7$ K.

Number (n)	Calculation ($\omega_{0,n}$)	S_n	Letter symbol	Experiment ($\omega_{0,n}$)	HoMnO$_3$ (γ_n)	S_n
1	102	0.08	A	123.5	1.4	0.26
2	199	1.33	B	223.0	4.0	2.8
3	235	0.34	C	256.0	4.9	0.4
4	361	0.045	D	298.1	5.8	0.3
5	393	0.018				
6	427	0.066				
7	486	0.133	E	486.1	10.7	2.1
8	620	0.001				
9	654	3.25	F	580.5	13.5	2.2
						$\varepsilon_{\infty,\parallel} = 4.88$

close to zero regardless of the sample thickness. Nevertheless, the phonons that are close to 420, 530, and 590 cm^{-1} have been confirmed in the transmission experiments, but the accuracy of our ellipsometry data for these weak modes is much superior compared to the transmission approach.

Above the spectral region dominated by the first-order phonon excitations (<600 cm^{-1}), transmission spectra demonstrated a number of peaks that can be attributed to multiphonon absorption. Figure 12 shows transmission spectra obtained at different temperatures in LuMnO$_3$. While other compounds have similar spectra, LuMnO$_3$ has been chosen for illustration due to the absence of the $4f^{3+}$ transitions in R^{3+} ions. A number of absorption peaks between 650 and 850 cm^{-1} correspond to the phonon density of states for two-phonon excitations, while the weaker absorption peaks in the range between 900 and 1150 cm^{-1} are probably due to three-phonon absorption. The two-phonon frequencies at $T = 7$ K are the following: 660, 702, 721, 751, 771, 791, 809, 818, 841, and 851 cm^{-1}. The three-phonon peaks are at 941, 967, 1004, 1030, 1073, 1138 cm^{-1}. Note that the peaks are much sharper at low temperatures, and their frequencies decrease as the temperature increases. This trend is expected for the phonon-related absorption and is also illustrated in Fig. 12 for the peak at 751 cm^{-1}.

IV. DISCUSSION AND CONCLUSIONS

First, we have to mention that only 6 out of expected 9 c axis polarized phonons and 13 out of 14 phonons polarized in the ab plane were observed experimentally. This fact could be understood from the analysis of vibration-induced dipole momenta: for both A_1 and E_1 symmetries, there are several modes whose oscillator strengths $S_{n(m)}$ are expected to be rather small (less than 0.05, see Tables V and VI). Such weak oscillator strength, especially if combined with a significant broadening $\gamma_{n(m)}$ of more than 5 cm^{-1}, can indeed result in an experimental situation in which the mode falls below the observation limit, especially if it occurs in proximity with other strong phonons of the same polarization.

Further, there is a reasonable agreement between the experimental and calculated mode frequencies, as shown in Tables III and IV for HoMnO$_3$. For example, the model reproduces qualitatively the general trend of phonon frequency change upon variation of the R^{3+} ion (Tables V and VI). As far as calculated oscillator strengths are concerned, the agreement with experiment deteriorates, which could point towards deficiency of a simplified shell model. These facts confirm the importance of a proper accounting for a balance among electronic, magnetic, and lattice degrees of freedom and highlight the importance of systematic experimental

TABLE V. Calculated frequencies and oscillator strengths for TO phonons with the E_1 symmetry.

Number (m)	HoMnO$_3$ ($\omega_{0,m}$)	S_m	ErMnO$_3$ ($\omega_{0,m}$)	S_m	YbMnO$_3$ ($\omega_{0,m}$)	S_m
1	125	0.1	121	0.102	117	0.112
2	166	0.001	167	0.001	166	0.0001
3	196	0.001	198	0.001	197	0.001
4	276	0.01	277	0.001	277	0.001
5	286	0.14	288	0.14	288	0.134
6	370	2.89	377	2.78	382	2.7
7	398	0.02	400	0.001	407	0.046
8	415	0.04	423	0.033	429	0.031
9	429	0.18	435	0.223	441	0.26
10	561	0.35	579	0.61	590	0.81
11	570	1.55	589	1.3	600	1.14
12	571	0.001	581	0.013	601	0.001
13	609	0.001	617	0.001	623	0.0014
14	667	0.02	673	0.001	683	0.001

TABLE VI. Calculated frequencies and oscillator strengths for TO phonons with the A_1 symmetry.

Number (n)	HoMnO$_3$ ($\omega_{0,n}$)	S_n	ErMnO$_3$ ($\omega_{0,n}$)	S_n	YbMnO$_3$ ($\omega_{0,n}$)	S_n
1	102	0.081	107	0.08	109	0.08
2	199	1.33	205	1.25	208	1.2
3	235	0.34	245	0.45	250	0.48
4	361	0.045	363	0.046	364	0.046
5	393	0.018	397	0.008	400	0.004
6	427	0.066	434	0.063	438	0.063
7	486	0.133	490	0.148	493	0.146
8	620	0.001	625	0.001	629	0.0002
9	654	3.25	661	3.24	671	3.24

information on optical properties and vibrational spectra of this class of materials.

In conclusion, we have measured the optical phonons in five h-RMnO$_3$ compounds. The majority of the optical phonons have been identified for the *ab* plane. The six strongest phonons that are polarized along the *c* axis have been observed in HoMnO$_3$. The lowest frequency phonons with the E_1 symmetry show a systematic variation with the mass of the corresponding R^{3+} ions. Two of the midfrequency phonons with the E_1 symmetry also show a systematic variation, which is determined by the systematic change of the R^{3+} ionic radius. The spin-phonon interaction has been observed in all h-RMnO$_3$ compounds in a form of the frequency increase for the phonons associated with displacement of the Mn^{3+} ions. The weakest effect was observed in HoMnO$_3$, while the other four h-RMnO$_3$ compounds have more pronounced spin-phonon interaction effects. The Grüneisen parameter $\gamma_G = 0.7 \pm 0.2$ has been determined for the strong phonons with the E_1 symmetry in all measured h-RMnO$_3$ compounds. Magnetic excitations at $\sim$190 cm^{-1} have been found in three of the h-RMnO$_3$ compounds at the temperature range below the AFM phase transition. These excitations have been explained as due to the two-magnon density of states. A possible relationship of this magnetic excitation to the crystal field transitions has been ruled out by both the close proximity of the frequencies in three h-RMnO$_3$ compounds and by observation of such excitation in LuMnO$_3$ where the $4f$ shell of the R^{3+} ion is fully occupied. The experimental and theoretical data presented here will be useful for future studies of the phonon spectra in a broad class of hexagonal magnetic compounds, and in new materials, such as h-InMnO$_3$ in particular.

[1] J. A. Alonso, M. J. Martinez-Lope, M. T. Casais, and M. T. Fernandez-Diaz, Inorg. Chem. **39**, 917 (2000).

[2] J.-S. Zhou, J. B. Goodenough, J. M. Gallardo-Amores, E. Moran, M. A. Alario-Franco, and R. Caudillo, Phys. Rev. B **74**, 014422 (2006).

[3] S. Petit, F. Moussa, M. Hennion, S. Pailhès, L. Pinsard-Gaudart, and A. Ivanov, Phys. Rev. Lett. **99**, 266604 (2007).

[4] H. Katsura, N. Nagaosa, and A. V. Balatsky, Phys. Rev. Lett. **95**, 057205 (2005).

[5] I. A. Sergienko and E. Dagotto, Phys. Rev. B **73**, 094434 (2006).

[6] M. Mostovoy, Phys. Rev. Lett. **96**, 067601 (2006).

[7] Y. Tokura, J. Magn. Magn. Mater. **310**, 1145 (2007).

[8] C. Kadlec, V. Goian, K. Z. Rushchanskii, P. Kužel, M. Ležaič, K. Kohn, R. V. Pisarev, and S. Kamba, Phys. Rev. B **84**, 174120 (2011).

[9] D. Talbayev, A. D. LaForge, S. A. Trugman, N. Hur, A. J. Taylor, R. D. Averitt, and D. N. Basov, Phys. Rev. Lett. **101**, 247601 (2008).

[10] S. C. Abrahams, Acta Crystallogr. Sect. B **57**, 485 (2001).

[11] V. Goian, S. Kamba, C. Kadlec, D. Nuzhnyy, P. Kužel, J. Agostinho Moreira, A. Almeida, and P. B. Tavares, Phase Transitions **83**, 931 (2010).

[12] M. N. Iliev, H.-G. Lee, V. N. Popov, M. V. Abrashev, A. Hamed, R. L. Meng, and C. W. Chu, Phys. Rev. B **56**, 2488 (1997).

[13] I. Munawar and S. H. Curnoe, J. Phys.: Condens. Matter **18**, 9575 (2006).

[14] S. H. Kim, S. H. Lee, T. H. Kim, T. Zyung, Y. H. Jeong, and M. S. Jang, Cryst. Res. Technol. **35**, 19 (2000).

[15] H. Fukumura, S. Matsui, H. Harima, K. Kisoda, T. Takahashi, T. Yoshimura, and N. Fujimura, J. Phys.: Condens. Matter **19**, 365239 (2007).

[16] L. Martín-Carrón and A. de Andrés, Phys. Rev. Lett. **92**, 175501 (2004).

[17] L. Martín-Carrón, A. de Andrés, M. J. Martínez-Lope, M. T. Casais, and J. A. Alonso, Phys. Rev. B **66**, 174303 (2002).

[18] H. Fukumura, N. Hasuike, H. Harima, K. Kisoda, K. Fukae, T. Takahashi, T. Yoshimura, and N. Fujimura, J. Phys.: Conf. Ser. **92**, 012126 (2007).

[19] H. Fukumura, N. Hasuike, H. Harima, K. Kisoda, K. Fukae, T. Yoshimura, and N. Fujimura, J. Phys.: Condens. Matter **21**, 064218 (2009).

[20] J. Liu, C. Toulouse, P. Rovillain, M. Cazayous, Y. Gallais, M.-A. Measson, N. Lee, S. W. Cheong, and A. Sacuto, Phys. Rev. B **86**, 184410 (2012).

[21] Anirban Ghosh, Jyoti Ranjan Sahu, S. Venkataprasad Bhat, and C. N. R. Rao, Solid State Sci. **11**, 1639 (2009).

[22] J. Vermette, S. Jandl, A. A. Mukhin, V. Yu. Ivanov, A. Balbashov, M. M. Gospodinov, and L. Pinsard-Gaudart, J. Phys.: Condens. Matter **22**, 356002 (2010).

[23] A. P. Litvinchuk, M. N. Iliev, V. N. Popov, and M. M. Gospodinov, J. Phys.: Condens. Matter **16**, 809 (2004).

[24] N. Thi Minh Hien, X.-B. Chen, L. Huy Hoang, D. Lee, S.-Y. Jang, T. W. Noh, and I.-S. Yang, J. Raman Spectrosc. **41**, 983 (2010).

[25] N. Thi Minh Hien, S.-Y. Oh, X.-B. Chen, D. Lee, S.-Y. Jang, T. W. Noh, and I.-S. Yang, J. Raman Spectrosc. **42**, 1774 (2011).

[26] X.-B. Chen, N. Thi Minh Hien, D. Lee, S-Y. Jang, T. W. Noh, and I.-S. Yang, New J. Phys. **12**, 073046 (2010).

[27] J. Vermette, S. Jandl, and M. M. Gospodinov, J. Phys.: Condens. Matter **20**, 425219 (2008).

[28] C. Toulouse, J. Liu, Y. Gallais, M.-A. Measson, A. Sacuto, M. Cazayous, L. Chaix, V. Simonet, S. de Brion, L. Pinsard-Godart, F. Willaert, J. B. Brubach, P. Roy, and S. Petit, Phys. Rev. B **89**, 094415 (2014).

[29] M. Zaghrioui, V. Ta Phuoc, R. A. Souza, and M. Gervais, Phys. Rev. B **78**, 184305 (2008).

[30] B. Souchkov, J. R. Simpson, M. Quijada, H. Ishibashi, N. Hur, J. S. Ahn, S. W. Cheong, A. J. Millis, and H. D. Drew, Phys. Rev. Lett. **91**, 027203 (2003).

[31] S.-T. Lou, F. M. Zimmermann, R. A. Bartynski, N. Hur, and S.-W. Cheong, Phys. Rev. B **79**, 214301 (2009).

[32] J. M. Wesselinowa and St. Kovachev, J. Phys.: Condens. Matter **19**, 386218 (2007).

[33] St. Kovachev and J. M. Wesselinowa, J. Phys.: Condens. Matter **22**, 255901 (2010).

[34] A. Prikockytė, D. Bilc, P. Hermet, C. Dubourdieu, and P. Ghosez, Phys. Rev. B **84**, 214301 (2011).

[35] J. Varignon, S. Petit, A. Gellé, and M. B. Lepetit, J. Phys.: Condens. Matter **25**, 496004 (2013).

[36] E. F. Bertaut and M. Mercier, Phys. Lett. **5**, 27 (1963).

[37] P. A. Sharma, J. S. Ahn, N. Hur, S. Park, Sung Baek Kim, Seongsu Lee, J.-G. Park, S. Guha, and S-W. Cheong, Phys. Rev. Lett. **93**, 177202 (2004).

[38] S. G. Condran and M. L. Plumer, J. Phys.: Condens. Matter **22**, 162201 (2010).

[39] B. Lorenz, A. P. Litvinchuk, M. M. Gospodinov, and C. W. Chu, Phys. Rev. Lett. **92**, 087204 (2004).

[40] B. G. Ueland, J. W. Lynn, M. Laver, Y. J. Choi, and S.-W. Cheong, Phys. Rev. Lett. **104**, 147204 (2010).

[41] B. Lorenz, F. Yen, M. M. Gospodinov, and C. W. Chu, Phys. Rev. B **71**, 014438 (2005).

[42] B. Lorenz, ISRN Condens. Matter Phys. **2013**, 497073 (2013).

[43] A. Munoz, J. A. Alonso, M. J. Martinez-Lope, M. T. Casais, J. L. Martinez, and M. T. Fernandez- Diaz, Chem. Mater. **13**, 1497 (2001).

[44] T. Lonkai, D. Hohlwein, J. Ihringer, and W. Prandl, Appl. Phys. A **74**, S843 (2002).

[45] M. Fiebig, D. Frohlich, K. Kohn, S. Leute, T. Lottermoser, V. V. Pavlov, and R. V. Pisarev, Phys. Rev. Lett. **84**, 5620 (2000).

[46] M. Fiebig, D. Frohlich, T. Lottermoser, and K. Kohn, Appl. Phys. Lett. **77**, 4401 (2000).

[47] M. Fiebig, C. Degenhardt, and R. V. Pisarev, J. Appl. Phys. **91**, 8867 (2002).

[48] M. Fiebig, D. Frohlich, T. Lottermoser, and M. Maat, Phys. Rev. B **66**, 144102 (2002).

[49] X. Fabrèges, I. Mirebeau, P. Bonville, S. Petit, G. Lebras-Jasmin, A. Forget, G. André, and S. Pailhès, Phys. Rev. B **78**, 214422 (2008).

[50] H. A. Salama and G. A. Stewart, J. Phys.: Condens. Matter **21**, 386001 (2009).

[51] Y. Geng, N. Lee, Y. J. Choi, S.-W. Cheong, and W. Wu, Nano Lett. **12**, 6055 (2012).

[52] I. E. Dzyaloshinskii, Sov. Phys. JETP **10**, 628 (1960).

[53] T. Moriya, Phys. Rev. **120**, 91 (1960).

[54] E. Standard, T. Stanislavchuk, A. Sirenko, N. Lee, and S.-W. Cheong, Phys. Rev. B **85**, 144422 (2012).

[55] T. N. Stanislavchuk, T. D. Kang, P. D. Rogers, E. C. Standard, R. Basistyy, A. M. Kotelyanskii, G. Nita, T. Zhou, G. L. Carr, M. Kotelyanskii, and A. A. Sirenko, Rev. Sci. Instr. **84**, 023901 (2013).

[56] T. D. Kang, E. Standard, G. L. Carr, T. Zhou, M. Kotelyanskii, and A. A. Sirenko, Thin Solid Films **519**, 2698 (2011).

[57] G. D. Gale, J. Chem. Soc. Faraday Trans. **93**, 629 (1997).

[58] V. N. Popov, J. Phys.: Condens. Matter **7**, 1625 (1995).

[59] M. N. Iliev, M. V. Abrashev, A. P. Litvinchuk, V. G. Hadjiev, H. Guo, and A. Gupta, Phys. Rev. B **75**, 104118 (2007).

[60] G. E. Jellison, Jr. and J. S. Baba, J. Opt. Soc. Am. A **23**, 468 (2006).

[61] P. D. Rogers, T. D. Kang, T. Zhou, M. Kotelyanskii, and A. A. Sirenko, Thin Solid Films **519**, 2668 (2011).

[62] J. Ménéndez and M. Cardona, Phys. Rev. B **29**, 2051 (1984).

[63] A. P. Litvinchuk, J. Magn. Magn. Mater. **321**, 2373 (2009).

[64] T. Penney, P. Berger, and K. Kritiyakirana, J. Appl. Phys. **40**, 1234 (1969).

[65] J. Oh, M. D. Le, J. Jeong, J.-H. Lee, H. Woo, W.-Y. Song, T. G. Perring, W. J. L. Buyers, S.-W. Cheong, and J.-G. Park, Phys. Rev. Lett. **111**, 257202 (2013).

[66] Y. J. Choi, N. Lee, P. A. Sharma, S. B. Kim, O. P. Vajk, J. W. Lynn, Y. S. Oh, and S-W. Cheong, Phys. Rev. Lett. **110**, 157202 (2013).